Comparative study on IWO and ICO transparent conductive oxide films prepared by reactive plasma deposition for copper electroplated silicon heterojunction solar cell

Huan Liu[1,2] (ID), Yuanbo Gong[3], Hongwei Diao[1], Xiaojie Jia[1], Lei Zhao[1,2,4,*], Wenjing Wang[1,2,4], Wei Wang[3], and Jun Zong[3]

[1] *Key Laboratory of Solar Thermal Energy and Photovoltaic System of Chinese Academy of Sciences, Institute of Electrical Engineering Chinese Academy of Sciences, Beijing 100190, China*

[2] *University of Chinese Academy of Sciences, Beijing 100049, China*

[3] *SPIC Central Research Institute, Beijing 102209, China*

[4] *Dalian National Laboratory for Clean Energy, The Chinese Academy of Sciences, Dalian 116023, China*

ABSTRACT

Reactive plasma deposition (RPD) was utilized to prepare W-doped In_2O_3 (IWO) and Ce-doped In_2O_3 (ICO) transparent conductive oxide (TCO) films for fabricating the copper electroplated silicon heterojunction (C-HJT) solar cell. TCOs with high carrier mobility (μ_e) and low carrier concentration (N_e) are preferred for the solar cell to limit the photocurrent loss induced by the possible free carrier absorption in TCOs. The electrical and optical properties of the IWO and ICO films were optimized via adjusting the RPD process conditions. As a result, both IWO and ICO films presented higher μ_e and lower N_e than the Sn-doped In_2O_3 (ITO) control prepared by magnetron sputtering. Especially, the ICOs could achieve much higher μ_e. When an optimized ICO with μ_e of up to 101.7 cm^2/V s was applied on the back side of the C-HJT solar cell, about 0.5% relative enhancement for the efficiency of the solar cell was achieved. The superior electrical and optical properties of ICO films are conducive to the improvement of cell efficiency.

1 Introduction

Silicon heterojunction (HJT) solar cell becomes more and more popular due to its low temperature budget, high efficiency, no light-induced degradation, and low temperature coefficient [1–3]. The representative front to back structure of the HJT solar cell is as the following: metal grid/TCO/a-Si:H(n$^+$)/a-Si:H(i)/c-Si(n)/a-Si:H(i)/a-Si:H(p)/TCO/metal grid, where TCO is the transparent conductive oxide film to

Address correspondence to E-mail: zhaolei@mail.iee.ac.cn

facilitate the lateral current transport to the metal grid. There are many types of TCO films, most of which are based on indium oxide (In_2O_3) or zinc oxide (ZnO) doped with various metal elements such as Sn, W, Mo, Ce, Al, and so on. [4–6]. The commonly used one is ITO (In_2O_3 doped with SnO_2) due to its good electrical and optical properties [7, 8]. However, when ITO is applied on the HJT solar cell, the relatively severe free carrier absorption resulted from its high carrier concentration can lower the current generation of the solar cell in the near infrared light range.

Since the conductivity of TCO (σ) is determined by the product of its carrier concentration (N_e) and mobility (μ_e), some novel TCOs with low N_e and high μ_e are developed to inhibit the possible free carrier absorption, such as W-doped In_2O_3 (IWO) and Ce-doped In_2O_3 (ICO). The typical N_e and μ_e of IWO, ICO, and ITO obtained by the worldwide studies are summarized in Table 1 and are also depicted in Fig. 1 for more clear distinction. Obviously, both IWO and ICO present lower N_e and higher μ_e than ITO overall. However, it is still difficult to determine which of IWO and ICO is the better, since the reference data are achieved from different sources and distribute with great overlapping. At the same time, reactive plasma deposition (RPD) has been recognized as a preferred way to deposit excellent TCOs compared with physical vapor deposition (PVD), since the TCOs prepared by RPD has a denser structure, higher crystallinity, smoother surface, higher conductivity, and better optical transmittance [4, 9]. Also, due to the lower ion energy in RPD, the damage to the amorphous silicon layer is reduced. Additionally, for the HJT solar cell fabrication, instead of the common Ag grid electrode formed by screen-printing, copper grid electrode formed by electroplating is considered as an effective alternative to reduce the grid width and the material cost [10].

Here, we comparatively investigated the fabrication of IWO and ICO films on the same RPD equipment. The electrical and optical properties of the two kinds of TCO films were optimized via adjusting the process conditions. As a result, it demonstrated that the optimized ICO had higher μ_e than the optimized IWO. Then, the application potential of the ICO film was explored on the copper electroplated silicon heterojunction (C-HJT) solar cell by comparing to the traditional ITO film control.

2 Experimental

RPD (Archers RPD-1Gun) was adopted to deposit the IWO and ICO films on glass substrates with the targets composed of 99.0% In_2O_3: 1.0% WO_3 in weight and 97.0% In_2O_3: 3.0% CeO_2 in weight, respectively. A large number of studies have shown that these two ratios of targets exhibit excellent performance [5, 11, 12, 22]. The performance of the TCOs was optimized systematically via adjusting the RPD process conditions, including the O_2 concentration (the percentage of O_2 in the total amount of O_2 and Ar) in the range of 11.3–42.9%, the current density of the plasma gun in the range of 145–175 A/m^2, and the deposition pressure in the range of 1.0–4.0 mTorr. The ITO control was deposited by magnetron sputtering (XEA∣nova, Vonardenne) with the target composed of 95.0% In_2O_3: 5.0% SnO_2 in weight, which shows good performance in cell applications due to its lower carrier concentration and better conductivity compared to other ratios of TCO [8, 29]. The condition was optimized in advance as follows: the temperature of 150 °C, the sputtering power density of 0.13 W/cm^2, and the deposition pressure of 3.0 mTorr. By adjusting the deposition time for each condition, the thicknesses of all the obtained TCO films on glass substrates were controlled to be about 100 nm, which matches the thickness required on the cell. A post-deposition annealing treatment was utilized to modify all the TCO films' performance by annealing at 210 °C for 50 min in the air. Such annealing treatment could simulate the subsequent thermal process after the Cu electrode electroplating and it is consistent with the low temperature conditions of the cell preparation process. For the C-HJT solar cell fabrication, n-type crystalline silicon wafers (size: M2; thickness: ∼ 180 μm; resistivity: 0.5–3.5 Ω cm) were utilized. The wafers were cleaned and textured firstly, resulting in the randomly distributed pyramidal texture with the size of ∼ 2 μm and the averaged surface reflectivity of ∼ 11%. Then the ∼ 5 nm a-Si:H(i), ∼ 7 nm a-Si:H(p) and ∼ 6 nm a-Si:H(n) layers were deposited by 13.56 MHz radio frequency (RF) plasma-enhanced chemical vapor deposition (PECVD) with the chamber pressure as 1.0 Torr and the substrate temperature as about 200 °C. Afterward, 80 nm-thick TCO films were prepared on both sides of the cells, followed by the copper electroplating to prepare the metal grid electrodes with 9-busbar pattern. For the solar cell with ITO control, both the front and back

Table 1 The typical carrier concentration (N_e) and the mobility (μ_e) of IWO/ICO/ITO films obtained by different preparation methods (RPD, PVD, and others) from references

TCO type	Preparation method	μ_e (cm²/V s)	N_e (× 10^{20} /cm³)	Target ratio	Data source
IWO	RPD	122	2.35	$In_2O_3:WO_3$ = 99:1	Shen et al. [11]
	RPD	89	1.6	$In_2O_3:WO_3$ = 99:1	Meng et al. [12]
	RPD	85	1.0	$In_2O_3:WO_3$ = 99:1	Meng et al. [13]
	RPD	82	1.7	$In_2O_3:WO_3$ = 99:1	Koida et al. [14]
	RPD	77.8	2.37	$In_2O_3:WO_3$ = 97:3	Lu et al. [15]
	RPD	77.8	2.86	$In_2O_3:WO_3$ = 99:1	Yu et al. [4]
	RPD	65.2	1.5	$In_2O_3:WO_3$ = 99:1	Huang et al. [16]
	PVD	73	2.9	$In_2O_3:WO_3$ = 97.8:2.2	Abe et al. [17]
	PVD	57	4	$In_2O_3:WO_3$ = 96:4	Li et al. [18]
	Pulsed laser deposition	112	2.5	$In_2O_3:WO_3$ = 97:3	Newhouse et al. [19]
ICO	RPD	133.8	2.1	$In_2O_3:CeO_2$ = 97:3	Shi et al. [20]
	PVD	100	2.6	$In_2O_3:CeO_2$ = 98:2	Tutsch et al. [21]
	PVD	71.2	2.01	$In_2O_3:CeO_2$ = 97:3	Dey et al. [22]
	PVD	51.6	2.11	$In_2O_3:CeO_2$ = 97:3	An et al. [5]
	PVD	50	2.5	$In_2O_3:CeO_2$ = 97:3	Kang et al. [23]
	Ion plating	130	2	No parameters	Watabe et al. [24]
	Ion plating	80	2	$In_2O_3:CeO_2$ = 97:3	Kobayashi et al. [6]
	Precursor solution	56	0.833	3.7% Ce	Kim et al. [25]
ITO	RPD	50	10	$In_2O_3:SnO_2$ = 95:5	Meng et al. [13]
	PVD	56	1.4	$In_2O_3:SnO_2$ = 90:10	Wang et al. [26]
	PVD	45.1	2.4	$In_2O_3:SnO_2$ = 90:10	Bhorde et al. [27]
	PVD	44	5.5	$In_2O_3:SnO_2$ = 90:10	Kang et al. [23]
	PVD	40	1.57	$In_2O_3:SnO_2$ = 50:50	Voisin et al. [28]
	PVD	32	2.2	$In_2O_3:SnO_2$ = 95:5	Valla et al. [29]
	PVD	28	7.7	$In_2O_3:SnO_2$ = 95:5	Krajangsang et al. [7]
	PVD	28	10	$In_2O_3:SnO_2$ = 90:10	Sousa et al. [8]
	PVD	26.3	3.61	$In_2O_3:SnO_2$ = 90:10	An et al. [5]
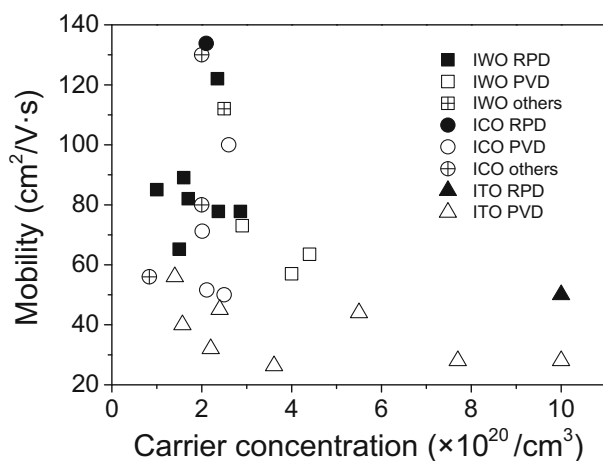
Fig. 1 The typical carrier concentration (N_e) and the mobility (μ_e) of IWO/ICO/ITO films obtained by different preparation methods (RPD, PVD, and others) from references [4–8, 11–23, 25–29]

TCOs were composed of a single ITO layer, as shown in Fig. 2a. For the solar cell with new TCO developed here, as shown in Fig. 2b, the front TCO was still the above single ITO layer, but the 70 nm-thick outer part of the back ITO was replaced by the new TCO. That was, the back TCO became a bi-layer film with 10 nm ITO/70 nm new TCO. The 10 nm-thick inner ITO was kept to avoid the direct contact between the new TCO and the underneath a-Si:H(p), since the ITO/a-Si:H(p) contact had been optimized well. Thus, the new TCO/a-Si:H(p) contact issue could be unconcerned. Similarly, by applying the new TCO only onto the back side of the solar cell, the concern could be focused on the free carrier absorption effect of the TCO since only long-wavelength light could reach the back side.

For the TCO films formed on glass substrates, the optical transmittance was measured in the

Fig. 2 The structure of C-HJT solar cells **a** with the complete 80 nm single layer of ITO, **b** with the optimized ICO in the bi-layer structure of 10 nm ITO/70 nm ICO on the cell back side
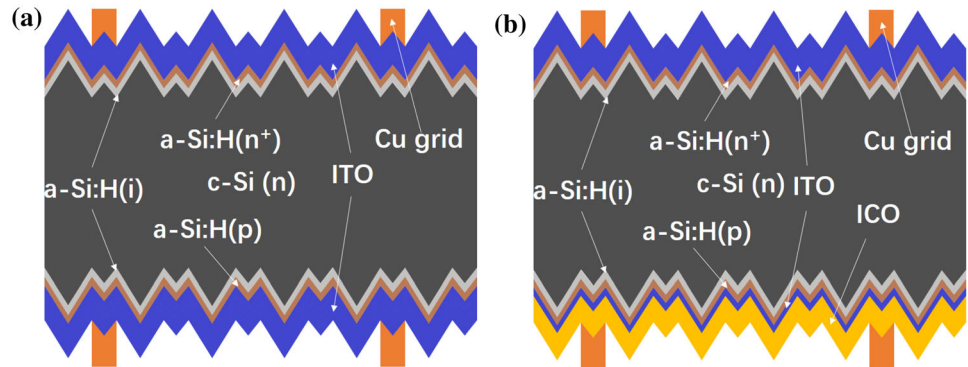

wavelength range of 300–1200 nm via ultraviolet–visible spectrophotometer (UV-2600), the thickness was obtained via ellipsometer (Raditech SE-950), and the resistivity (ρ), the carrier concentration (N_e), and the mobility (μ_e) were acquired via Hall measurement (Swin HALL8800-II). Further, the film crystallinity was analyzed via X-ray diffractometer (XRD D8 ADVANCE). For the C-HJT solar cells, a current–voltage (I–V) tester (PV-GS902L) was utilized to check the I–V performance under the standard test condition (AM1.5G, 1000 W/m^2, 25 °C). Quantum efficiency (QE) tester (QE-R666) was utilized to obtain the external quantum efficiency (EQE) and reflectivity (R), and the internal quantum efficiency (IQE) was calculated by EQE and R. The interfacial contact resistivity (ρ_c) of TCO/Cu was measured by transfer length method (TLM) [30].

3 Results and discussion

Figure 3 shows the electrical properties of the IWO and ICO films obtained under different O$_2$ concentrations during the RPD process as deposited and after annealing. The corresponding values of the optimized ITO control film are also presented. It can be seen that the resistivity of the annealed ITO control is about 9.6×10^{-4} Ω cm with the mobility up to 24.1 cm^2/V s and the carrier concentration of about 2.7×10^{20}/cm^3. Although ITO with lower resistivity can be prepared, its N_e will be too much higher to moderate the free carrier absorption effect. Comparing to the ITO control, both IWO and ICO demonstrate lower resistivity with the lowest values at intermediate O$_2$ concentrations. The annealing treatment can improve the conductance greatly, especially for the ICOs. Clearly, with the increase of O$_2$ concentration, the carrier concentration continuously

decreases and the mobility behaves reversely. Hence, when the O$_2$ concentration is low, the relatively higher resistivity can be attributed to the lower μ_e and when the O$_2$ concentration is high, the relatively higher resistivity should result from the lower N_e. The resistivity of ICOs is lower than that of IWOs mainly because of the higher μ_e. The transmittance spectra of the annealed IWO and ICO films in Fig. 4 further demonstrate that the transparency of the new TCOs is improved apparently when the O$_2$ concentration is high. The averaged transmittance can be up to close 90% for both IWOs and ICOs. For the optimized ITO control, when the wavelength is longer than 760 nm, its transmittance is obviously lower than that of the optimized IWOs and ICOs, which indicates that the lower N_e for the new TCOs indeed reduces the free carrier absorption effect.

In the TCO films, the carrier concentration is mainly provided by the effective doping ions and O vacancies [31]. As the O$_2$ concentration increases during the RPD process, O atoms incorporate into the film more and more, which results in a decrease of the O vacancies and the carrier concentration. The carrier mobility depends on the lattice vibration, neutral impurity scattering, ionized impurity scattering, and grain boundary scattering [32, 33]. When the O$_2$ concentration during deposition is low, the film quality is relatively poor with a great amount of O vacancies and defects. Such lattice vibration can lower the mobility. At the same time, as shown in Fig. 5, XRD analysis clearly demonstrates that the crystallinity of the film can be improved as the O$_2$ concentration increases during the RPD process. This result is the same as reported in the literature [9, 34]. The diffraction curves are consistent with the standard XRD spectrum of In$_2$O$_3$ (JCPDS No.06-0416), indicating that no new compounds are formed and
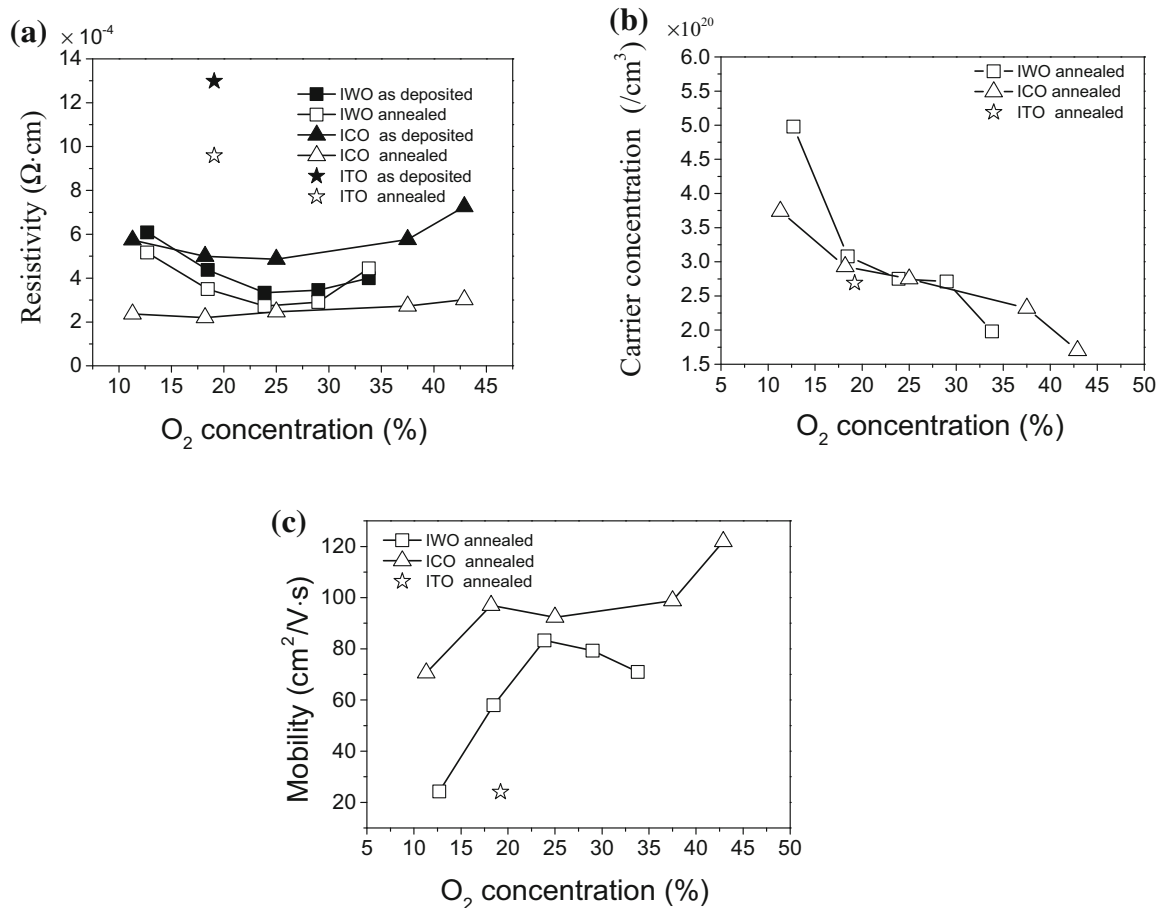
Fig. 3 **a** The resistivity (ρ) of IWO and ICO films obtained before and after annealing, **b** the carrier concentration (N_e), and **c** the carrier mobility (μ_e) of the annealed IWO and ICO films as functions of the O$_2$ concentration during the RPD process. The corresponding values of the optimized ITO control are also drawn for comparison
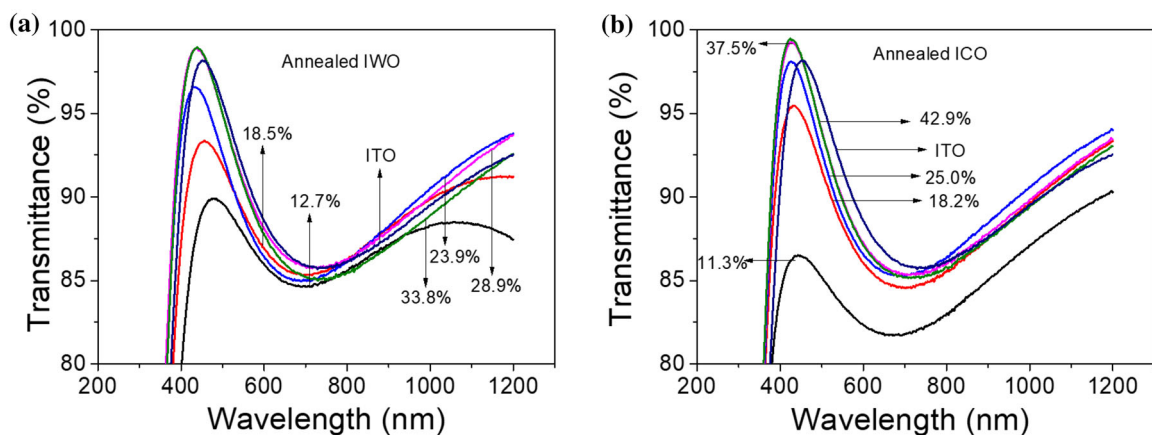
Fig. 4 The transmittance spectra of **a** the annealed IWO and **b** the annealed ICO films in the wavelength range of 300–1200 nm for the different O$_2$ concentrations during the RPD process. The O$_2$ concentrations are marked in the figure. The corresponding curve of the optimized ITO control is also drawn for comparison

the film is polycrystalline. For both IWO and ICO films, (222) is the main crystal plane. Because the (222) crystal plane has the lowest surface energy, the film tends to grow preferentially on the (222) crystal plane [35]. It also indicates W or Ce doping does not change the fundamental microstructure of In_2O_3. W and Ce atoms replace in atoms into the indium oxide lattice. The ITO film has relatively weak diffraction peaks, indicating that the crystallinity is relatively poor.

The grain size corresponding to the (222) diffraction peak can be quantitatively characterized according to the Scherrer formula as follows:

$$D = \frac{K\gamma}{B\cos\theta} \qquad (1)$$

where K is the Scherrer constant ($K = 0.89$), D is the average thickness (nm) of the crystal grain perpendicular to the crystal plane, B is the full width at half maximum (FWHM) of the diffraction peak, θ is the diffraction angle, and γ is the X-ray wavelength ($\gamma = 1.54$ Å).

The calculated D data are shown in Fig. 5c. Obviously, the grain size increases as a function of the O_2 concentration during the RPD process. ITO film has a smaller grain size than IWO and ICO films. The small grain size when the O_2 concentration is low leads to a strong grain boundary scattering and thus a low mobility. With the increase of O_2 concentration, the film quality improves and the grain size becomes larger. As a result, the lattice vibration and the grain boundary scattering are both reduced, leading to the increase of the mobility. By comparing Fig. 5a and b, it can also be found that the IWOs have more diffraction peaks than ICOs, which means that ICO has a more homogeneous crystalline orientation. Because the ionic radius of W^{6+} is 0.06 nm, Ce^{4+} is 0.087 nm, and In^{3+} is 0.08 nm, the lattice matching of Ce and In is better [15], resulting in ICO with a more
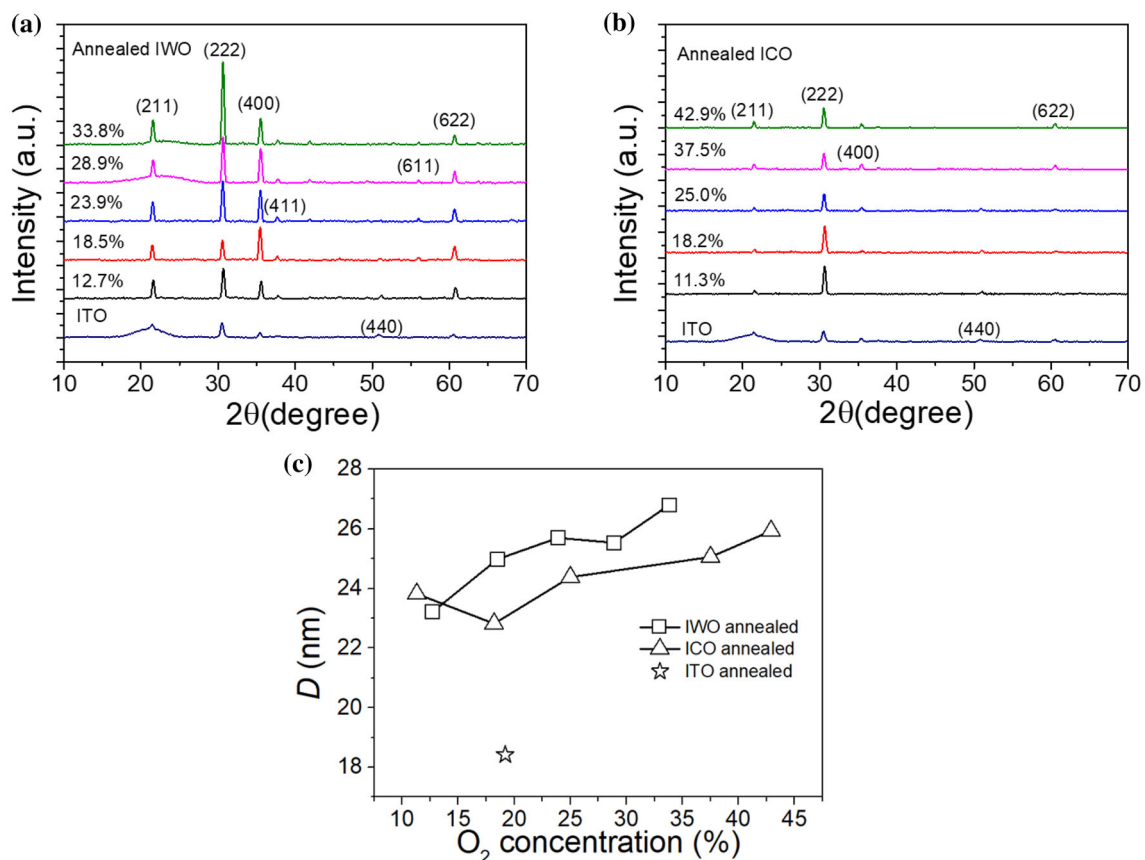
Fig. 5 The crystallinity analysis on the annealed IWO and ICO films obtained with different O_2 concentrations during the RPD process. a XRD curves of IWO films, b XRD curves of ICO films, c the corresponding grain size (D) calculated for the IWO and ICO films. The O_2 concentrations are marked in the figure. The corresponding results of the optimized ITO control are also drawn for comparison

homogeneous crystalline orientation. The parallel orientation of the crystalline grains can further reduce the grain boundary scattering. This should be one reason why the ICOs present higher mobility than the IWOs.

From the above results, it is found that the O_2 concentration has an important influence on the electrical properties, optical properties, and structure of the film. The microstructure with homogenous crystallization and relatively large grains would be helpful to improve the TCO performance. Similar to the variation of the O_2 concentration during the RPD process, the performance of the IWO and ICO films was further optimized by changing the current density of the plasma gun, the pressure of chamber, the annealing temperature, and time to modify the film microstructure. All the obtained results are shown in Fig. 6. The open squares represent ICO films, the solid squares represent IWO films, and the five-pointed star represents the ITO control film, respectively. It can be concluded that the optimized ICO films can have higher mobility and lower carrier concentration than the optimized IWO films. The mobility greater than 100 cm^2/V s with the carrier concentration lower to about $2.0 \times 10^{20}/cm^3$ can be easily obtained for ICOs. When the current density of the plasma gun is 160 A/m^2, the pressure of chamber is 1.0 mTorr and post-deposition annealing treatment is performed at 210 °C for 50 min in the air, the highest mobility of the obtained ICO film is up to 121.9 cm^2/V s with the carrier concentration of about

$1.7 \times 10^{20}/cm^3$, resulting in a resistivity of about 3.0×10^{-4} Ω cm. The low carrier concentration can guarantee the averaged transmittance close to 90.0% in the wide wavelength range of 300–1200 nm.

A representative ICO film with the mobility of 101.7 cm^2/V s, the carrier concentration of about $2.0 \times 10^{20}/cm^3$, and the resistivity of about 3.1×10^{-4} Ω cm was utilized for the C-HJT solar cell on the back side to replace the ITO film partially as described in experimental section. The I–V performance of the solar cells with ICO and ITO, respectively, is shown in Fig. 7. To make the comparison clear, data normalization is adopted referring to the averaged values of the cells with complete ITO, for which the short-circuit current density (J_{SC}) is 38.5 mA/cm^2, the open-circuit voltage (V_{OC}) is 0.738 V, the fill factor (FF) is 0.84, and the efficiency (E_{ff}) is 23.8%. As expected, when the ITO is replaced by the ICO mostly, about 1.0% relative enhancement for the J_{SC} is obviously achieved. However, the V_{OC} and the FF are relatively reduced about 0.25%. All these together result in a relative efficiency increase of about 0.5%.

As shown in Fig. 8, the IQE results show that the IQE of ICO is higher than that of ITO at long wavelength from 1000 to 1100 nm, which proves that the J_{SC} increase can be attributed to the contribution of the reduced free carrier absorption effect due to the lower N_e in the utilized ICO. Since the ICO also processes lower resistivity than the ITO control, the back bi-layer ITO/ICO film should demonstrate lower sheet resistance than the back single ITO film. So there must be other factors resulting in the FF decrease for the solar cells with ICO. The ρ_c measurement of TCO/Cu by TLM shows that ρ_c of ICO/Cu is 0.128 Ω cm^2 but ρ_c of ITO/Cu is only 0.098 Ω cm^2. It can be generally believed that the high ρ_c of ICO/Cu is one main reason for the above FF reduction. The slight decrease of V_{OC} might be induced by the ITO microstructure fluctuation due to its thickness reduction. So if strategies to modify the above V_{OC} and FF-related issues are further explored, the contribution of the adoption of ICO with high μ_e and low N_e to enhance the efficiency of the C-HJT solar cell should be much greater.
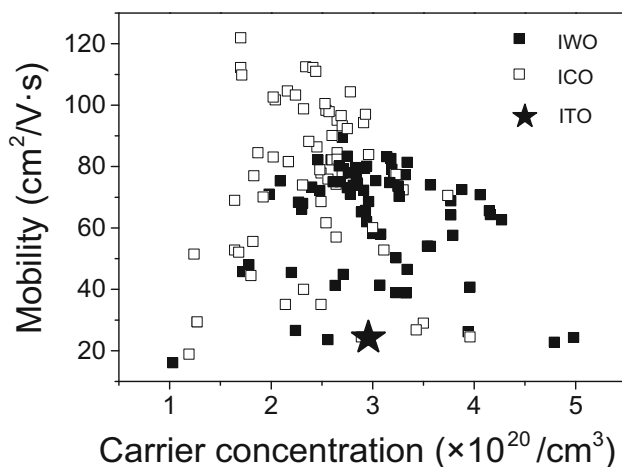
Fig. 6 The carrier concentration (N_e) and the mobility (μ_e) of the annealed IWO and ICO films obtained by various RPD process conditions. The corresponding results of the optimized ITO control are also drawn for comparison

Fig. 7 The *I–V* performance comparison of the C-HJT solar cells with the optimized ICO and ITO on the back side via adopting the bi-layer structure of 10 nm ITO/70 nm ITO or ICO. J_{SC} short-circuit current density, V_{OC} open-circuit voltage, *FF* fill factor, E_{ff} efficiency
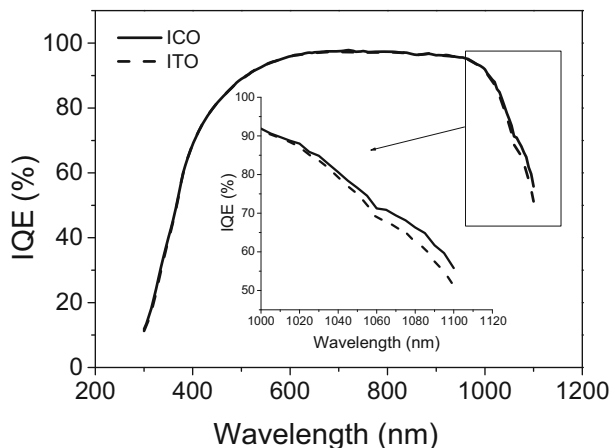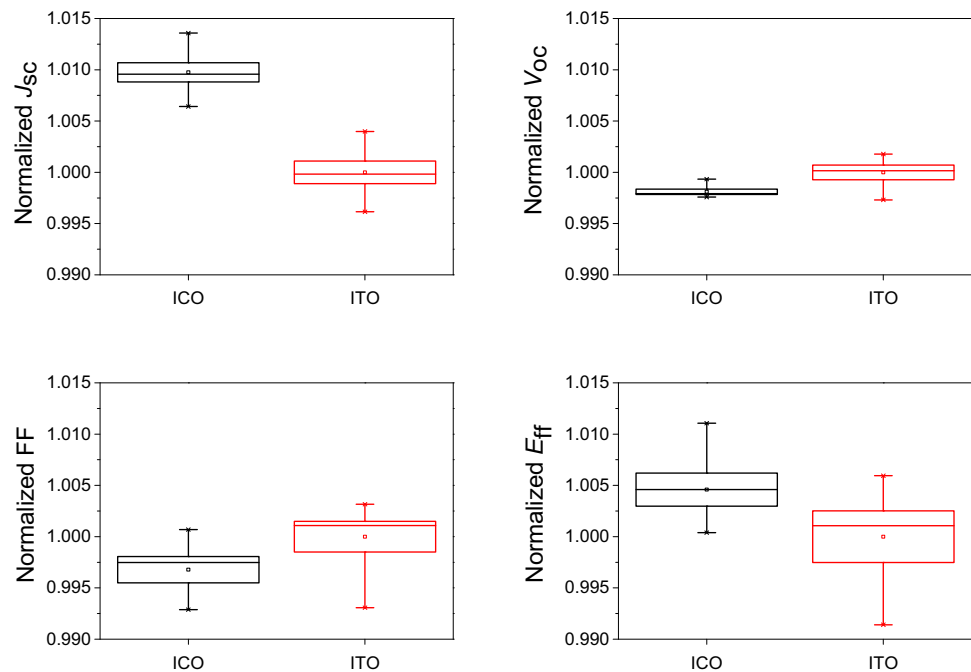
Fig. 8 The IQE performance comparison between the C-HJT solar cells with the optimized ICO in the bi-layer structure of 10 nm ITO/70 nm ICO and with the complete 80 nm single layer of ITO on the cell back side

cm^2/V s, N_e: about 2.7×10^{20}/cm^3) for the back TCO film on the C-HJT solar cell. As a result, about 0.5% relative enhancement for the efficiency of the solar cell was achieved. Comparing to the low ρ_c of ITO/Cu, high ρ_c of ICO/Cu was considered as one main factor to lower FF of the solar cell. The slight decrease of V_{OC} might be attributed to the ITO microstructure fluctuation due to its thickness reduction. Hence, the strategies to modify the V_{OC} and FF issues should be explored further, and thus the adoption of ICO could enhance the efficiency of the C-HJT solar cell more greatly.

4 Conclusion

By investigating the influence of the O$_2$ concentration during the deposition on the structure, and the electrical and optical properties of the obtained IWO and ICO films, it was revealed that the microstructure with homogenous crystallization and relatively large grains was helpful to improve the performance of the TCOs. As a demonstration, a representative ICO (μ_e: about 101.7 cm^2/V s, N_e: about 2.0×10^{20}/cm^3) was utilized to replace the ITO control (μ_e: about 24.1

Data availability

The datasets generated during and/or analyzed during the current study are available from the corresponding author on reasonable request.

Declarations

Conflict of interest   The authors have no relevant financial or non-financial interests to disclose.

References

1. B. Sarma, D. Barman, B.K. Sarma, Appl. Surf. Sci. **479**, 786–795 (2019)
2. B.L. Zhu, J.M. Ma, K. Lv, C.J. Wang, J. Wu, Z.H. Gan, J. Liu, X.W. Shi, Superlattices Microstruct. **140**, 106456 (2020)
3. H. Ferhati, F. Djeffal, K. Kacha, A. Bendjerad, A. Benhaya, Physica E: Low Dimens. Syst. Nanostruct. **106**, 25–30 (2019)
4. J. Yu, J. Bian, W. Duan, Y. Liu, J. Shi, F. Meng, Z. Liu, Sol. Energy Mater. Sol. Cells **144**, 359–363 (2016)
5. S. An, P. Chen, F. Hou, Q. Wang, H. Pan, X. Chen, X. Lu, Y. Zhao, Q. Huang, X. Zhang, Sol. Energy **196**, 409–418 (2020)
6. E. Kobayashi, Y. Watabe, T. Yamamoto, Y. Yamada, Sol. Energy Mater. Sol. Cells **149**, 75–80 (2016)
7. T. Krajangsang, V. Thongpool, C. Piromjit, K. Sriprapha, Opt. Mater. **101**, 109743 (2020)
8. M.G. Sousa, A.F. da Cunha, Appl. Surf. Sci. **484**, 257–264 (2019)
9. K.-Y. Chen, S.-P. Chang, C.-H. Lin, RSC Adv. **9**, 87–90 (2019)
10. C. Han, Y.F. Zhao, L. Mazzarella, R. Santbergen, A. Montes, P. Procel, G.T. Yang, X.D. Zhang, M. Zeman, O. Isabella, Sol. Energy Mater. Sol. Cells **227**, 111082 (2021)
11. L. Shen, Shanghai Institute of Microsystem and Information Technology, Chinese Academy of Sciences **69** (2016)
12. F. Meng, J. Shi, Z. Liu, Y. Cui, Z. Lu, Z. Feng, Sol. Energy Mater. Sol. Cells **122**, 70–74 (2014)
13. F. Meng, J. Shi, L. Shen, L. Zhang, J. Liu, Y. Liu, J. Yu, J. Bao, Z. Liu, Jpn. J. Appl. Phys. **56**, 120 (2017)
14. T. Koida, J. Nishinaga, Y. Ueno, H. Higuchi, H. Takahashi, M. Iioka, Y. Kamikawa, H. Shibata, S. Niki, Prog. Photovolt. **27**, 491–500 (2019)
15. Z. Lu, F. Meng, Y. Cui, J. Shi, Z. Feng, Z. Liu, J. Phys. D: Appl. Phys. **46**, 075103 (2013)
16. W. Huang, J. Shi, Y. Liu, F. Meng, Z. Liu, J. Alloys Compd. **843**, 155151 (2020)
17. Y. Abe, N. Ishiyama, Mater. Lett. **61**, 566–569 (2007)
18. X. Li, Q. Zhang, W. Miao, L. Huang, Z. Zhang, Thin Solid Films **515**, 2471–2474 (2006)
19. P.F. Newhouse, C.H. Park, D.A. Keszler, J. Tate, P.S. Nyholm, Appl. Phys. Lett. **87**, 3 (2005)
20. J. Shi, F. Meng, J. Bao, Y. Liu, Z. Liu, Mater. Lett. **225**, 54–56 (2018)
21. L. Tutsch, H. Sai, T. Matsui, M. Bivour, M. Hermle, T. Koida, Prog. Photovolt. **29**, 835–845 (2021)
22. K. Dey, A.G. Aberle, S. van Eek, S. Venkataraj, Ceram. Int. **47**, 1798–1806 (2021)
23. S. Kang, S. Cho, P. Song, Thin Solid Films **559**, 92–95 (2014)
24. Y. Watabe, E. Kobayashi, in 29th European Photovoltaic Solar Energy Conference and Exhibition (2014), pp. 472–474
25. B.H. Kim, C.M. Staller, S.H. Cho, S. Heo, C.E. Garrison, J. Kim, D.J. Milliron, ACS Nano **12**, 3200–3208 (2018)
26. J.Q. Wang, C.C. Meng, L. Zhao, W.J. Wang, X.X. Xu, Y.Z. Zhang, H. Yan, Sol. Energy **204**, 720–725 (2020)
27. A. Bhorde, A. Jadhavar, R. Waykar, S. Nair, H. Borate, S. Pandharkar, R. Aher, D. Naik, P. Vairale, G. Lonkar, S. Jadkar, Thin Solid Films **704**, 137972 (2020)
28. L. Voisin, M. Ohtsuka, S. Petrovska, R. Sergiienko, T. Nakamura, Optik **156**, 728–737 (2018)
29. A. Valla, P. Carroy, F. Ozanne, D. Muñoz, Sol. Energy Mater. Sol. Cells **157**, 874–880 (2016)
30. D.K. Schroder, L.G. Rubin, Phys. Today **44**, 107–108 (1991)
31. L.S. Jianhua Shi, F. Meng, Z. Liu, Mater. Lett. **182**, 32–35 (2016)
32. Z.L. Pei, C. Sun, M.H. Tan, J.Q. Xiao, D.H. Guan, R.F. Huang, L.S. Wen, J. Appl. Phys. **90**, 3432–3436 (2001)
33. E. Shanthi, V. Dutta, A. Banerjee, K.L. Chopra, J. Appl. Phys. **51**, 6243–6251 (1980)
34. J. Shi, L. Shen, F. Meng, Z. Liu, Mater. Lett. **182**, 32–35 (2016)
35. S. Ahn, S. Kim, V.A. Dao, S. Lee, S.M. Iftiquar, D. Kim, S.Q. Hussain, H. Park, J. Lee, Y. Lee, J. Cho, S. Kim, J. Yi, Thin Solid Films **546**, 342–346 (2013)

Publisher's Note   Springer Nature remains neutral with regard to jurisdictional claims in published maps and institutional affiliations.